Supporting Information

Meghana et al. 10.1073/pnas.1018652108

SI Text

Theoretical Considerations. ***Estimation of cellular prestress.*** The early (<200 s) isotropic cell expansion of the ablated cell of size R provides us with a quantitative estimate of the prestress (Fig. 1*E*, main text). The isotropicity of the expansion implies that the prestress $\sigma^{(\mathrm{pre})}$ is released as an isotropic excess pressure. Assuming free expansion at these early times, force balance requires that the driving force is equal to viscous dissipation, which we assume occurs primarily between AS cells. This implies $\nabla\cdot\sigma^{(\mathrm{pre})} \approx \eta\nabla^2 v$, where η is the AS cytoplasmic viscosity. On dimensional grounds, we replace the velocity v by the radial expansion rate $\dot{R}$ and so $\frac{\sigma^{(pre)}}{R} \approx \frac{\eta\dot{R}}{d^2}$, where d is the thickness of the membrane-cortical layer, giving rise to the linear expansion in cell area, $A \approx \frac{2\pi d^2\sigma^{(pre)}}{\eta}t$. The velocities we observe upon ablations compare well with a recent study (1) that makes a similar argument for the estimation of "prestress," albeit at the scale of a single cell.

Sequence of symmetry breaking shape transitions before delamination. In this section we provide a quantitative description of the shape deformations before delamination, in both the natural and induced situations. This allows us to identify the sequence of symmetry-breaking shape transitions that the neighboring cells undergo en route to eventual delamination of the central cell. Further, this characterization allows us to mathematically construct quantities that correspond to the consequences of the sequential deployment of active stress generators.

It is natural to represent the deformations of the apical shape of each cell by expanding the local shape $R(\theta,t)$ (where R, θ are the polar coordinates of a point on the contour of the cell surface with respect to a coordinate frame whose origin is at the centroid) in a harmonic series,

$$R(\theta,t) = r_0\left(1+\sum_{l=0}^{\infty} a_l(t)e^{il\theta}\right), \qquad [1]$$

where r_0 is the "radius" of the undeformed cell, and $a_l(t)$ the amplitudes representing the time-dependent deformations. The lowest deformation modes have simple physical meanings: for instance, $l = 0$ corresponds to isotropic expansion, $l = 1$ to centroid movement, $l = 2$ to elliptical distortions resulting in an aspect ratio or shape anisotropy, and finally $l = 3$ to the breaking of up/down (reflection) symmetry.

As described in the main text, the observable onset of natural delamination is marked by a "ring" of cells acquiring a significant shape anisotropy, characterized by an $l = 2$ symmetry-breaking transition, which leads to the rosette pattern surrounding the prospective delaminating cell. The subsequent appearance of the actomyosin collar in the neighboring cells at the interface with the delaminating cell, applies contractile forces that result in another symmetry-breaking shape deformation ($l = 3$ mode), characterized by the breaking of up/down (reflection) symmetry. This leads to a further strengthening of the rosette. As a consequence, the area of the delaminating cell starts decreasing with a rate proportional to $a_2{\cdot}a_3$, the product of the amplitudes of the $l = 2$ and 3 deformations of the neighboring cells. At this stage, the neighboring cells produce polarized microtubules, the microscopic generators of the force dipoles associated with each cell. This results in a finite radial centroid velocity with respect to the substrate. The centroid movement corresponds to an $l = 1$ deformation; the corresponding velocity can be seen to be $\frac{da_1}{dt} \propto a_2{\cdot}a_1$. The velocity vectors around the delaminating cell point radially inward in the form of an aster, which gets progressively more well defined, resulting in a faster contraction of the delaminating cell leading to its ultimate extrusion.

Theoretical proposal based on active hydrodynamics. The essential idea we propose is that delamination is a process of mechanical yielding of a tissue at the site of the delaminating cell as a consequence of the deployment of active stress generators in the neighboring cells. A problem of physical interest is how we a priori identify the sites of delamination. Throughout this article we have taken the view that the delaminating cell is "selected" spontaneously as a result of a collective stress patterning in the tissue. The framework of active hydrodynamics, which has been applied to the study of mechanics of cells and tissues (2), is appropriate for the study of dorsal closure. Here we sketch how such a theory can be formulated in the context of dorsal closure, without going into a detailed exposition. In addition, we provide a physically motivated local criterion for mechanical yielding of the tissue. We leave more detailed calculations and comparison with experiments to later.

The process of dorsal closure can be viewed as the dynamics of a compacted (no voids) collection of cells constituting the amnioserosa (AS), confined within a moving boundary (leading edge of the epidermis). The stresses arising as a result of cell–cell contact, cell–substrate interaction, and active force generators (cytoskeletal elements, actin, and microtubules) give rise to shape deformation, cell movement, and occasionally cell loss (delamination). This in turn remodels the cell–cell contacts and the cytoskeleton. The boundary moves inward as a result of the force-generating cells at the periphery; the interior cells of the AS can thus be associated with a relative velocity with respect to the substrate, which is the sum of a mean flow toward the midline of the contracting AS and systematic deviations. As a result of the compaction constraint, the contraction is slow at first, then crosses over to a faster rate. Provided we focus on the central cells away from the periphery and study the dynamics during the slow contraction phase, we may ignore the effects of the boundary (Fig. 1, main text).

The dynamics of compacted active deformable cells of area Ω can be described in terms of a local cell density ρ, an active stress density $\sigma^{(a)}$, which in general has contributions from both cortical (predominantly cortical actin) and bulk stresses (arising predominantly from actomyosin and microtubules) and the shape deformation tensor $\overleftrightarrow{Q}$ obtained from Eq. **1** above. The dynamics of the density ρ obeys mass conservation, except when delamination occurs—the mass current has contributions from both the centroid velocity $\vec{n}$ of the cell and the active stress, $\sigma^{(a)}$. Delamination occurs whenever the local active stress exceeds a threshold, $\sigma^{(a)} > \sigma_c$, the yield criterion. To determine σ_c, we argue as follows: before the onset of delamination every cell–cell interface is subject to active cellular prestress and satisfies force balance. Delamination follows from an imbalance of forces at the surface of the delaminating cell and is associated among other things with cytoskeletal loss in the shrinking cell. Thus, this threshold stress must be of the order of the prestress. We have estimated the magnitude of the prestress in our subcellular ablation experiments (Fig. 1*E*, main text).

We wish to highlight two major differences between tissue dynamics in the AS and, say, in the wing imaginal disc. One is the possible significant role played by active cell body stresses (arising predominantly from polarized microtubules), measured by the

dimensionless parameter, $\Gamma \equiv \frac{\sigma_s^{(a)}\sqrt{\Omega}}{\sigma_b^{(a)}}$, the ratio of the body to surface stresses. This is in contrast to the wing imaginal disk (where Γ is low), which is believed to be driven by active contractile surface stresses arising from cortical actin (3, 4). The other is related to the low extent of cell–cell sliding (T1 process) in the AS, primarily as a result of high cell adhesion. On the other hand, significant cell movement happens upon delamination (T2 process). As we show here (Fig. 3, main text), improper adhesion influences the generation and polarization of active stresses and alters the dynamics of delamination. These results suggest that the genetic (in the entire tissue) or emergent (spatially within the same tissue as we see here) regulation of optimal adhesion is a critical determinant of differences in dynamics.

SI Materials and Methods. ***Genotypes analyzed.***

1. w;UbiDE-Cadherin GFP
2. w;UbiDE-Cadherin GFP/+; H2B eGFP/+
3. w;UAS α-catenin GFP armadillo Gal4
4. w;UAS actin5C GFP/+;; c^{381}Gal4/+
5. w;;mat α-tubulin Gal4 UAS EB1GFP/+
6. w;β-tubulin GFP
7. w;sqh GFP
8. w;UAS α-catenin GFP armadillo Gal4/+ ; UAS αPS3 RNAi/+
9. w;UAS actin5C GFP/+; UAS αPS3 RNAi/+; c^{381}Gal4/+
10. w;UAS actin5C GFP/+; UAS βPSRNAi/+; c^{381}Gal4/+
11. w;UbiDE-Cadherin GFP/+; UAS spastin eGFP/+; c^{381}Gal4/+
12. CsBz and w;;UAS EB1 GFP/+; c^{381} Gal4/+ (for immunofluorescence)
13. w;sqh GFP/+; UAS βPSRNAi/+; c^{381}Gal4/+
14. w;sqh GFP/+; UAS spastin eGFP/+; c^{381}Gal4/+
15. w; UAS Apoliner/ UAS α-catenin GFP armadillo Gal4
16. w; UAS α-catenin GFP armadillo Gal4/+; UAS p35/+

Imaging. A Zeiss confocal fluorescence microscope (LSM510-Meta NLO) with a Plan-Neofluar 40× 1.3-N.A. oil-immersion objective was used for imaging. Confocal images (512 × 512 pixels, 8-bit images) were acquired. EGFP was excited with the 488-nm line of an argon-ion laser (Lasos) and the emission collected with a 500- to 550-nm band-pass filter. Stacks of 5 μm were acquired with a step size of 1 μm. For live imaging, images were acquired at the rate of 3.93 s per frame (approximately three to five 3D frames per minute) with a 3.5× zoom.

For experiments in Figs. 4 *A–C* and 5 *D–G* (main text), a Zeiss confocal fluorescence microscope (LSM 710) with a Plan-Neofluar 63× 1.4-N.A. oil-immersion objective was used for imaging. Confocal images (512 × 512 pixels, 8-bit images) were acquired. EGFP was excited with the 488-nm line of an argon-ion laser (Lasos) and the emission collected with a 500- to 550-nm band-pass filter. Stacks of 7 μm were acquired with a step size of 0.5 μm. For live imaging, images were acquired at the rate of approximately three to five 3D frames per minute with a 1.5× zoom. Movies were generated on ImageJ, compressed using Fast Movie Processor 1.41 (Cinepak Codec by Radius), and are programmed to play at 15 frames per second.

Fixed preparations were acquired on a Zeiss 710 microscope on a 63× 1.4-N.A. oil objective or on Olympus FV1000 on a 60× 1.4-N.A. oil objective, and stacks were generated from slices at 0.3-μm intervals. For all images, levels were adjusted to include the area under the curve. Composites were assembled in Adobe Photoshop and imported into Adobe Illustrator.

Immunochemistry. Whole-mount staining of embryos was performed according to standard protocols as previously described (5). Primary antibodies were monoclonal mouse anti-tubulin (1:500) and rabbit anti pY (1:500). Alexa-Fluor 488-, Cy3-, or Cy5-conjugated secondary antibodies were used at 1:200. Rhodamine phalloidin was used to visualize actin (1:100). Fluorescent images were acquired on a Zeiss 710 confocal microscope.

For the immunostaining in Fig. 4 (main text), embryos were ablated as described above and imaged to the expansion phase. Single ablated embryos were fixed through standard protocols (5) and stained.

Quantitative morphological analysis. Morphological parameters were obtained using ImageJ with manual extraction of cell outlines. In all of the graphs, area and perimeter are normalized to the original values for perturbed delamination and to 700 s before the cell area is close to zero for natural delamination. This is because the absolute cell sizes show considerable variability even in stage-matched embryos. Axes lengths, strains, and centroid movements were calculated using custom routines in LabVIEW. For the quantification of shape deformations in the nearest neighbors of delaminating cells, strain anisotropy was measured as $\frac{\Delta l_{||} - \Delta l_{\perp}}{l_{||} + l_{\perp}}$, where $l_{||}$ is the axis length parallel and $l_{\perp}$ is the axis length perpendicular to the line connecting the centroids of the neighboring cell and the delaminating cell. Nearest neighbors' centroid displacements relative to the centroid of the delaminating cell (r/r_0) were computed as the radial distance between the two centroids (r) normalized to the initial distance (r_0). Aspect ratio (of the peripheral AS cell) was measured as ratio of length of major axis to minor axis, with the major axis set perpendicular and the minor axis parallel to the leading edge of the lateral epidermis. Circularity $\left(C = \frac{4\pi\, Area}{Perimeter^2}\right)$, which is 1 for a circular object and falls as the object becomes elliptical. Equivalently, we define shape anisotropy $S_A = \frac{l_{||} - l_{\perp}}{l_{||} + l_{\perp}} = 1 - C$, which is 0 for a circle and nonzero for elliptical objects. Curve fitting was done using OriginPro 8. Error bars represent SE of mean unless mentioned otherwise. Statistical analysis was done on GraphPad software.

1. Mayer M, Depken M, Bois JS, Jülicher F, Grill SW (2010) Anisotropies in cortical tension reveal the physical basis of polarizing cortical flows. *Nature* 467:617–621.
2. Joanny JF, Julicher F, Kruse K, Prost J (2007) Hydrodynamic theory for multicomponent activ epolar gels. *N J Phys* 9:422.
3. Farhadifar R, Röper JC, Aigouy B, Eaton S, Jülicher F (2007) The influence of cell mechanics, cell-cell interactions, and proliferation on epithelial packing. *Curr Biol* 17: 2095–2104.
4. Rauzi M, Verant P, Lecuit T, Lenne PF (2008) Nature and anisotropy of cortical forces orienting *Drosophila* tissue morphogenesis. *Nat Cell Biol* 10:1401–1410.
5. Narasimha M, Brown NH (2006) Confocal microscopy of *Drosophila* embryos. In *Cell Biology: A Laboratory Handbook*, ed Celis JE (Academic Press, San Diego), 3rd Ed, Vol 3, pp 77–86.

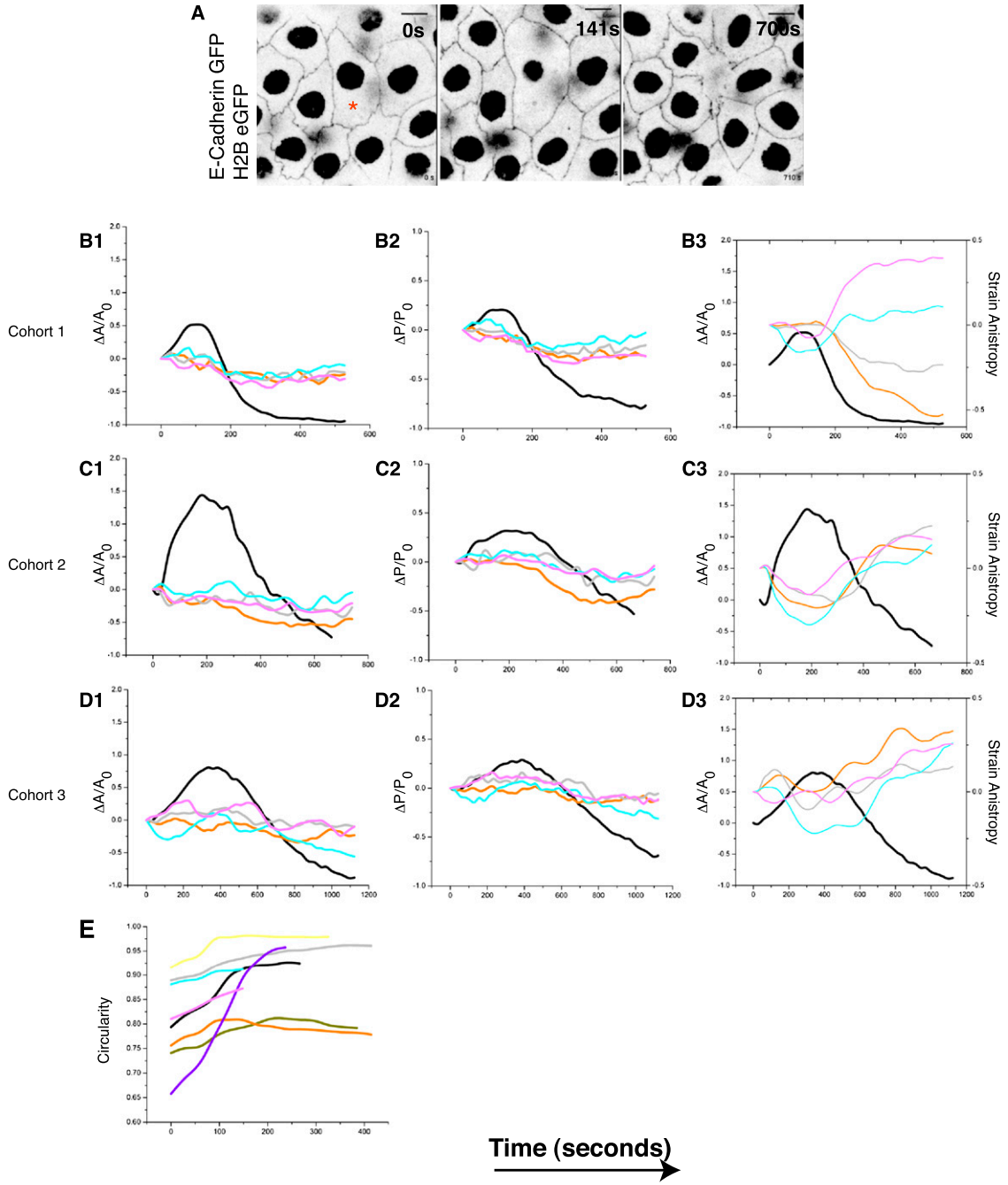

Fig. S1. Quantitative analysis of cell dynamics accompanying subcellular laser ablation-induced delamination. (*A*) Time-lapse confocal images of an embryo labeled with E-Cadherin-GFP to label the apical cell membrane and H2B eGFP to label the nucleus in response to subcellular cytoplasmic laser ablation. Asterisk marks perturbed cell. Fractional change in apical surface area (*B1–D1*) and perimeter (*B2–D2*) of the delaminating cell (black) and the nearest neighbors (colored) during natural delamination. Strain anisotropy dynamics of nearest neighbors (colored) with respect to the changing apical surface area of the delaminating cell (black) (*B3–D3*). Shape anisotropy dynamics of the delaminating cell as estimated by circularity (*E*) during the expansion phase of perturbed delamination. The parameters for individual neighbors are represented by the same color in all graphs. *B*, *C*, and *D* represent independent cohorts.

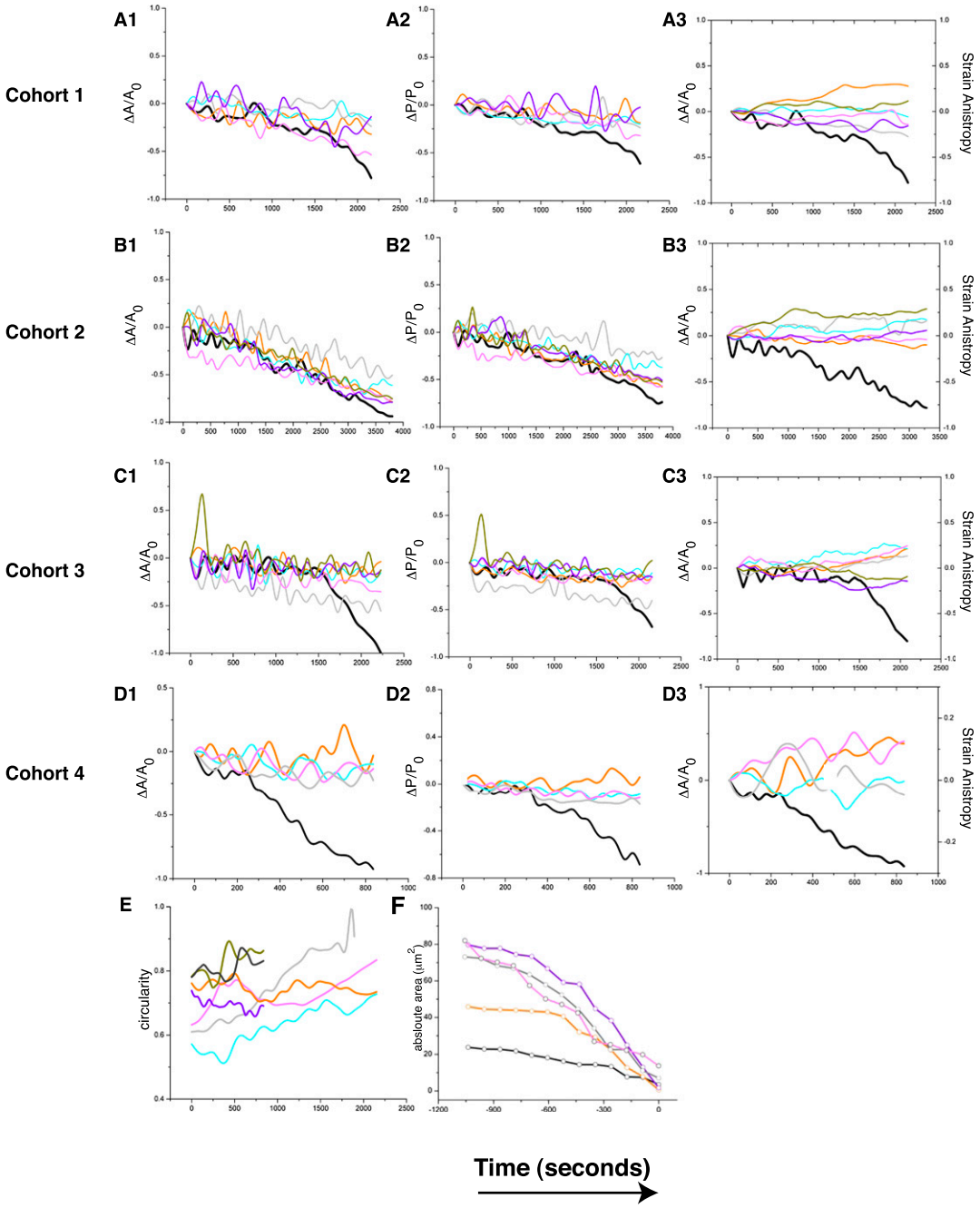

Fig. S2. Quantitative analysis of cell dynamics accompanying natural delamination. Fractional change in apical surface area (*A1–D1*) and perimeter (*A2–D2*) of the delaminating cell (black) and the nearest neighbors (colored) during natural delamination. Strain anisotropy dynamics of nearest neighbors (colored) with respect to the changing apical surface area of the delaminating cell (black) (*A3–D3*). The parameters for individual neighbors are represented by the same color in all graphs. *A*, *B*, *C*, and *D* represent independent cohorts. (*E*) Circularity of individual delaminating cells. (*F*) Absolute areas of individual delaminating cells.

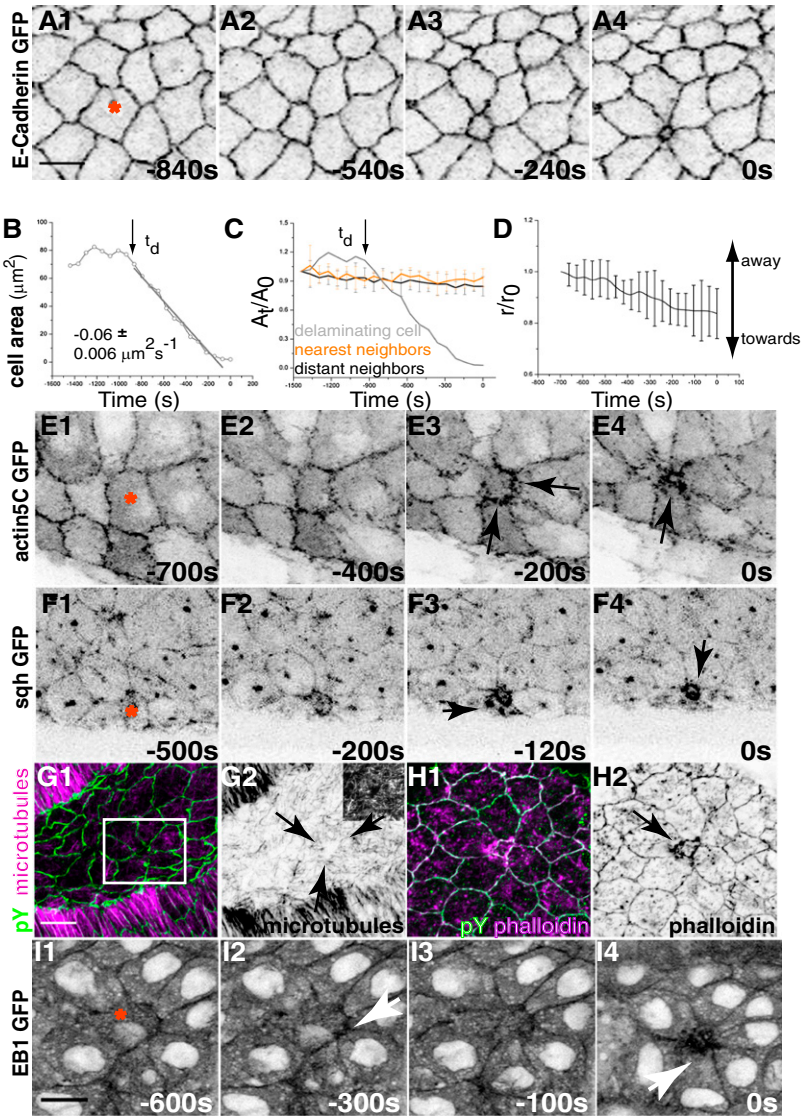

Fig. S3. Membrane and cytoskeletal dynamics associated with natural delamination. Time-lapse confocal images (*A1–A4*) and representative graph (*B*) showing apical area dynamics associated with natural delamination visualized with E-Cadherin GFP. t_d marks the onset of rapid area reduction. Linear fit with typical contraction rates indicated (n = 8; error represents SEM). (*C*) Representative graph depicting fractional change in apical surface area of a single central AS cell (DC, gray), its nearest neighbors (orange; n = 6), and distant neighbors (gray; n = 6). (*D*) Centroid displacement r/r0 of nearest neighbors with respect to DC (n = 10). Error bars represent SD. Time-lapse confocal images of embryos expressing actin5C GFP (*E1–E4*) or sqh GFP (*F1–F4*) during natural delamination. (*G* and *H*) Immunofluorescence on wild-type embryos against pY (green), tubulin (lilac in *G1*, gray in *G2*), and phalloidin (lilac in *H1* and gray in *H2*). Area in white box in *G1* is *Inset* in *G2*. (*I1–I4*) Time-lapse confocal images showing changes in microtubule cytoskeleton visualized by EB1 GFP (n = 3) during natural delamination. Asterisk indicates delaminating cell, and arrows point to polarized rearrangements. (Scale bars, 10 μm.)

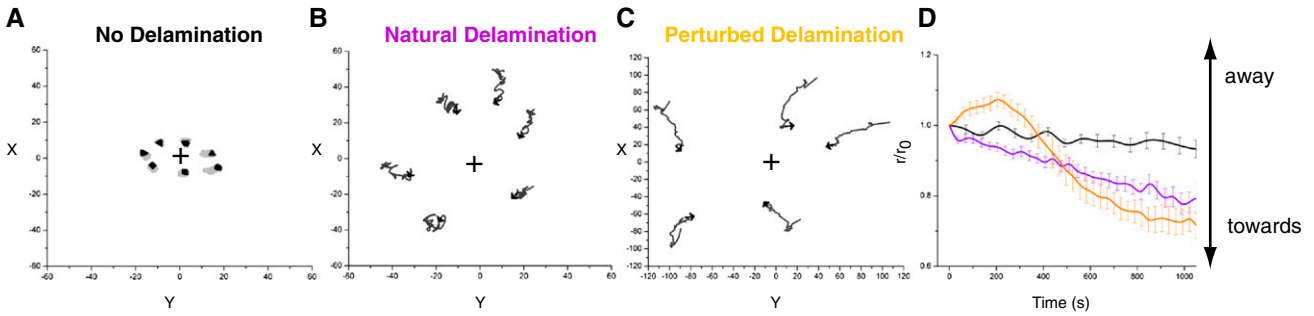

Fig. S4. Strain map associated with cellular delamination. Change in the centroid position of the neighboring cells with respect to the delaminating cell during natural (*B*) and perturbation-induced (*C*) delamination and in a non-delaminating rosette (*A*). The origin (+) represents the centroid position of the delaminating cell; black arrow represents end point of delamination. (*D*) Comparative dynamics of r/r0 in the neighbors surrounding a non-delaminating cell (black; n = 19 cells from three cohorts), a naturally delaminating cell (violet; n = 27 cells from five cohorts), and upon perturbation-induced delamination (orange; n = 9 cells from two cohorts).

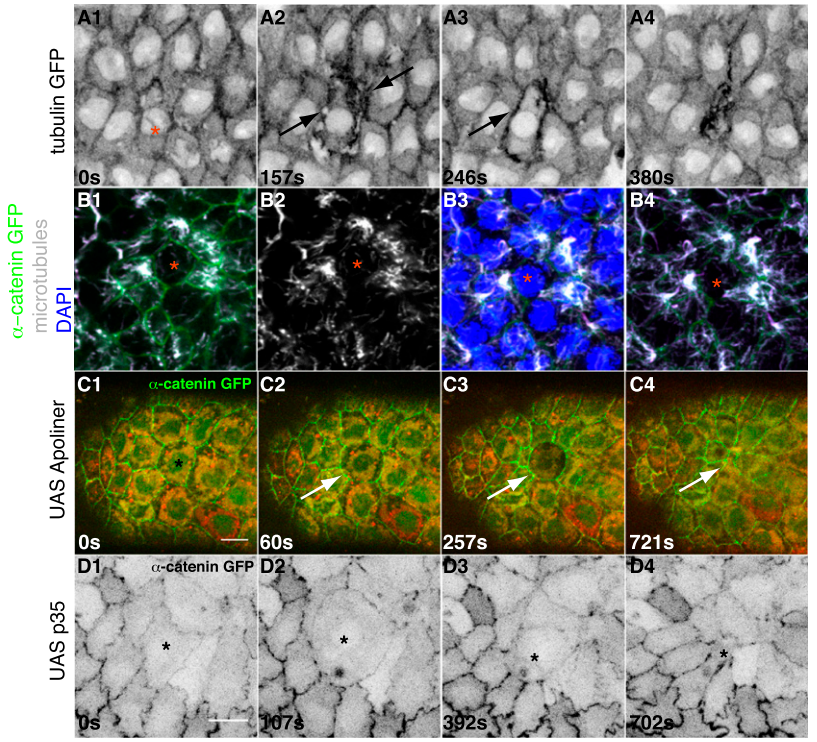

Fig. S5. Effect of subcellular cytoplasmic laser perturbation on the microtubule cytoskeleton and caspase activity. (*A1–A4*) Time-lapse confocal images showing changes in microtubule cytoskeleton visualized by β-tubulin GFP (n = 3). Arrows point to rearrangement of tubulin GFP. Single apical sections (*B1* and *B2*) and maximum intensity z-projections of a stack of confocal images (*B3* and *B4*) from embryos fixed after expansion, showing apical microtubule reorganization around the perturbed cell (white; α-catenin in green, DAPI in blue). Time-lapse confocal images of an embryo expressing the Apoliner transgene to show the absence of caspase activation (*C1–C4*; yellow cytoplasm) in the delaminating cell upon perturbation. The caspase inhibitor p35 (*D1–D4*) does not suppress the delamination in response to laser perturbation. Asterisks mark perturbed cell. (Scale bar, 10 μm.)

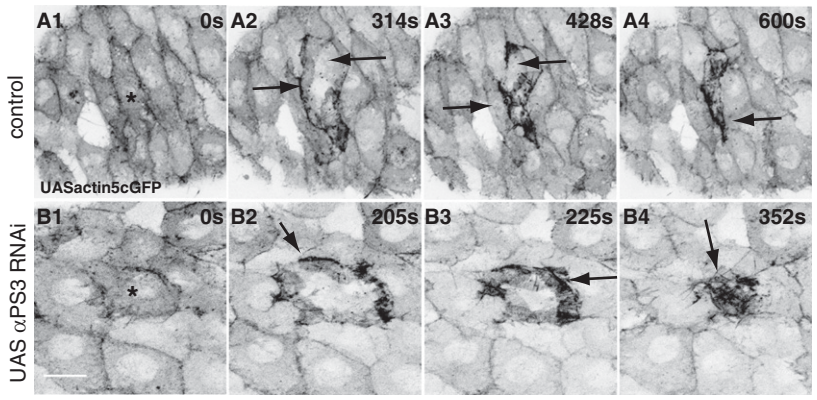

Fig. S6. Functional evidence for adhesion-dependant cytoskeletal remodeling in response to subcellular laser perturbation. Time-lapse confocal images showing the response of actin upon subcellular laser perturbation in control (*A*) and in mutants overexpressing αPS3 RNAi in the AS (*B*; $n = 10$). Arrows point to the rearrangement of actin. Asterisks indicate perturbed cell. (Scale bar, 10 μm.)

Table S1. Evolution of area dynamics upon induced delamination in control and mutant embryos

Variable	Control ($n = 8$)	αPS3RNAi ($n = 8$)	Control ($n = 8$)	Spastin ($n = 8$)
A_{max}	1.41 ± 0.05	1.68 ± 0.1	1.52 ± 0.07	1.31 ± 0.07
Time to A_{max} (s)	101.17 ± 12.27	183.58 ± 22.95*	112.54 ± 15.71	97.8 ± 12.38
Time to A_0 (s)	244.06 ± 22.92	358.04 ± 33.26*	279.35 ± 36.65	190.22 ± 22.12
Area at 700 s after ablation	0.00 ± 0.0	0.17 ± 0.03*	0.044 ± 0.029	0.151 ± 0.03*

Errors represent SEM.
*Significant difference ($P < 0.02$).

Table S2. Statistical analysis of cytoskeletal rearrangements in the absence of integrin function and microtubule integrity

Phenotype	Wild type [$n = 8$ (actin), $n = 5$ (myosin)]	αPS3 RNAi ($n = 10$)	βPS RNAi [$n = 5$ (both)]	Spastin overexpression ($n = 5$)
Time of onset of early myosin movement/ streaming (s)	61.46 ± 4.52		76.00 ± 3.5	Streams not visible
Time to cortical myosin enrichment (s)	220.1 ±17.08		497.5 ± 40.63	406.1 ± 56.6
Membrane ruffles/ lamellipodia during expansion	8	10	5	—
Cortical enrichment of actin during cell expansion	8	10	5	—
Cortical enrichment of actin during contraction	8	8	0	—
Spiky/ filopodia-like structures during cell expansion	2	8	5	—
Spiky structures during contraction	4 (≈3–4 spikes)	7	5	—
Apical extrusion	0	3	0	—
Delay in delamination (with respect to wild-type area at 800 s after ablation)	0	10	3	4

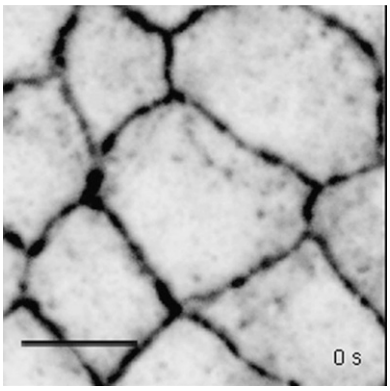

Movie S1. Subcellular laser perturbation in an embryo expressing E-Cadherin GFP.

Movie S1

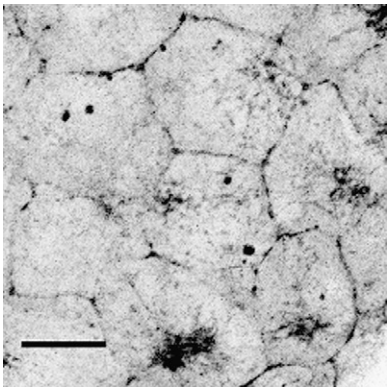

Movie S2. Subcellular perturbation in an embryo expressing a GFP fused to the non-muscle myosin II regulatory light chain (sqh GFP).

Movie S2

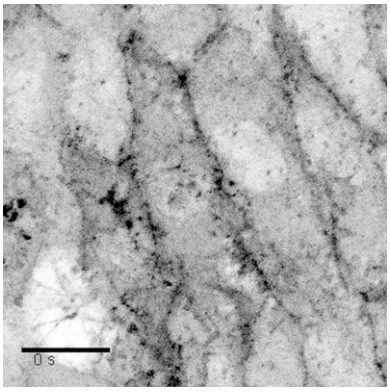

Movie S3. Subcellular cytoplasmic laser perturbation in an embryo expressing actin5C GFP in the AS.

Movie S3

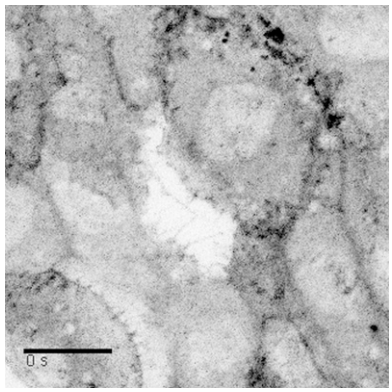

Movie S4. Subcellular cytoplasmic laser ablation in an embryo expressing actin5C GFP in the AS. The ablated cell does not express actin5C GFP.

Movie S4

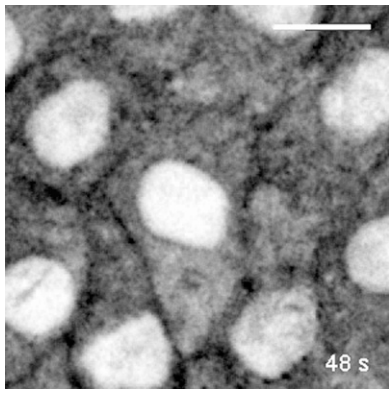

Movie S5. Subcellular cytoplasmic laser ablation in an embryo expressing EB1 GFP.

Movie S5

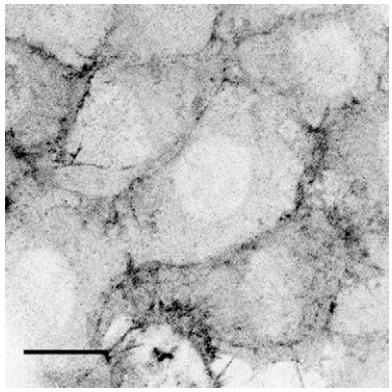

Movie S6. Altered delamination dynamics and actin reorganization upon perturbation in embryos overexpressing a βPS RNAi transgene in the AS visualized using actin5C GFP.

Movie S6

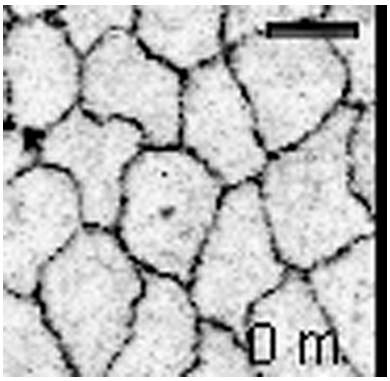

Movie S7. Natural delamination in an embryo expressing E-Cadherin GFP.

Movie S7

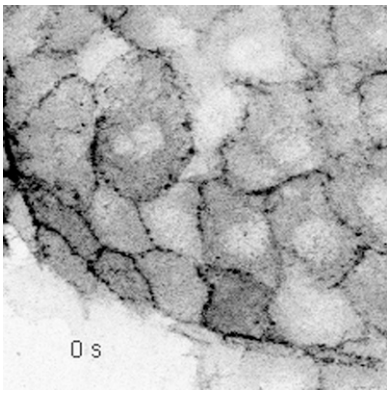

Movie S8. Natural delamination in an embryo expressing actin5C GFP in the AS.

Movie S8

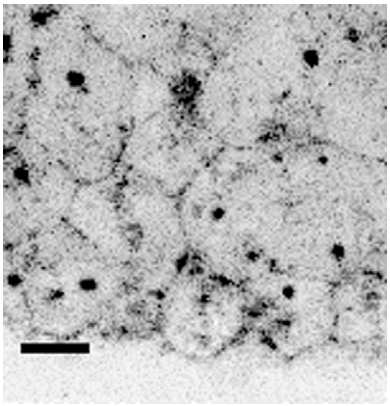

Movie S9. Natural delamination in an embryo expressing a sqh GFP.

Movie S9

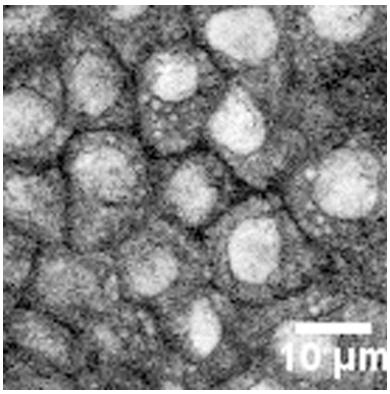

Movie S10. Natural delamination in an embryo expressing the microtubule plus end binding protein EB1 GFP in the AS.

Movie S10